The Astronomical Journal, 137:19–33, 2009 January
doi:10.1088/0004-6256/137/1/19

DYNAMICAL SIMULATIONS OF NGC 2523 AND NGC 4245

P. Treuthardt[1], H. Salo[2], and R. Buta[1]
[1] Department of Physics and Astronomy, University of Alabama, Box 870324, Tuscaloosa, AL 35487, USA
[2] Division of Astronomy, Department of Physical Sciences, University of Oulu, Oulu, FIN-90014, Finland
Received 2007 October 18; accepted 2008 September 14; published 2008 December 2

ABSTRACT

We present dynamical simulations of NGC 2523 and NGC 4245, two barred galaxies (types SB(r)b and SB(r)0/a, respectively) with prominent inner rings. Our goal is to estimate the bar pattern speeds in these galaxies by matching a sticky-particle simulation to the B-band morphology using near-infrared K_s-band images to define the gravitational potentials. We compare the pattern speeds derived by this method with those derived in our previous paper using the well-known Tremaine–Weinberg continuity equation method. The inner rings in these galaxies, which are likely to be resonance features, help to constrain the dynamical models. We find that both methods give the same pattern speeds within the errors.

Key words: galaxies: individual (NGC 2523, NGC 4245) – galaxies: kinematics and dynamics – galaxies: spiral

1. INTRODUCTION

The pattern speed, Ω_p, is one of the most influential and elusive parameters affecting the overall morphology of a galaxy. It remains one of the fundamental unknowns of galaxy dynamics. A variety of techniques for determining Ω_p have been published (e.g., Canzian 1993; Buta & Combes 1996; Puerari & Dottori 1997; Salo et al. 1999; Weiner et al. 2001; Egusa et al. 2004; Zhang & Buta 2007), though in recent years emphasis has been placed on an observational method developed by Tremaine & Weinberg (1984, hereafter TW). Studies of late that make use of this method have focused on estimating the pattern speed of SB0 galaxies (e.g., Aguerri et al. 2003; Corsini et al. 2003; Debattista et al. 2002). These studies have indicated that SB0 galaxies generally have "fast" bars, presumably indicating halos of low central concentration.

The TW method is the most direct means of measuring the pattern speed of a galaxy. Here, the pattern speed of a bar can be estimated from the luminosity weighted mean line-of-sight velocities, $\langle V\rangle$, and luminosity-weighted mean positions, $\langle X\rangle$ (both relative to the central values), of a tracer that obeys the continuity equation. These quantities are to be measured along lines parallel to a barred galaxy's projected-disk major axis (MA) and are related as follows:

$$\Omega_p \sin i = \frac{\langle V\rangle}{\langle X\rangle}, \qquad (1)$$

where i is the galaxy's inclination.

One of the great advantages of the TW method is that it provides pattern speeds independent of any assumptions concerning features traced by the pattern speed. For example, the TW method can be used to directly test the ideas that bars end near their own corotation resonances, and that rings are associated with specific resonances. However, this advantage is somewhat offset by the limited scope of applicability of the method. The most significant hindrance is that the bar MA must lie at approximately 45° to the MA of the projected disk in order to obtain the maximum TW signature strength, with angles between about 20° and 70° considered suitable (Gerssen et al. 2003). The galaxy itself must have a preferred inclination between 50° and 60° (Debattista 2003) in order to avoid large uncertainties. Another problem is identifying a pattern-speed tracer with a strong spectral signature that obeys the continuity equation. This means that the tracer must be something that is neither created nor destroyed and significant star formation would violate the equation. This is the reason that applications of this method to spirals have been more limited. Hernandez et al. (2005) discuss the application of the TW method to atomic, molecular, and ionized gas phases in spiral galaxies. SB0 galaxies were the first objects to which the method was applied, using stellar absorption lines (e.g., Merrifield & Kuijken 1995; Gerssen et al. 1999). These galaxies can have strong bar patterns but lack the dust and star formation that would complicate similar measurements for later-type systems. Recently though, a TW test of an n-body model by Gerssen & Debattista (2007) indicated that dust absorption effects may be partially mitigated by star formation on the leading edges of a bar, creating a minimal impact on the derived Ω_p. Avoiding these potentially problematic factors significantly diminishes the number of galaxies to which this method can be applied.

A less direct, yet more widely applicable method of determining Ω_p in galaxies is through simulation modeling (e.g., Salo et al. 1999; Rautiainen et al. 2005). This involves modeling the response of gas in a rigid galaxy potential, where the gas is modeled in terms of dissipatively colliding, or "sticky," particles. These sticky particles simulate the cold gas component of a galaxy, where regions of star formation occur due to cloud–cloud collisions (Levinson & Roberts 1981). The gravitational potential is derived from a near-infrared (NIR) image. Different dynamical parameters are varied until the morphology and kinematics of the numerically-simulated galaxy visually match, as closely as possible, the blue light morphology. The morphology of resonance rings is sensitive to the underlying pattern speed of a galaxy and serve as a good Ω_p estimator. We use deep B-band images with good resolution to compare the observed low-velocity dispersion components to our models. Since resonance rings generally form in the gas component and show emission from young stars, the observed B-band morphology is best suited for this purpose. Sticky-particle modeling is similar to hydrodynamic modeling, such as smoothed particle hydrodynamics (SPH), only the

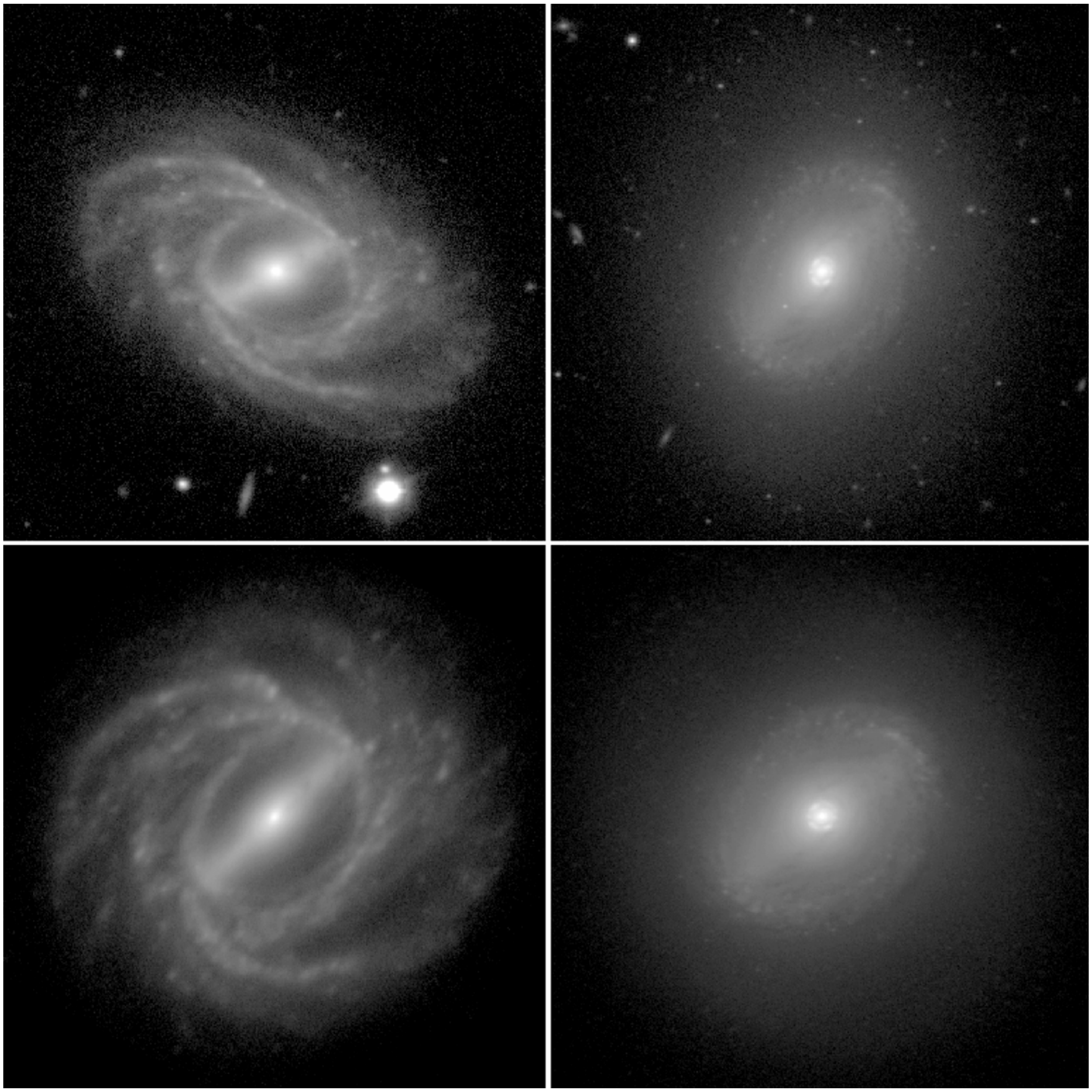

Figure 1. *B*-band images of NGC 2523 (left) and NGC 4245 (right). The upper images were obtained with the NOT in 2003 and 2004 (Laurikainen et al. 2005) and are presented as illustrated in the de Vaucouleurs Atlas of Galaxies (Buta et al. 2007). North is at the top and east is to the left in each case. The lower images are deprojected to the disk plane and have the foreground stars removed. The images are $3\farcm0 \times 3\farcm0$.

particles are not subjected to nongravitational forces. Therefore, the motions of particles are not affected by the positions of other particles (i.e., through pressure gradients), except through dissipation in physical impacts. This difference means that SPH is better suited for modeling the warm gas phase of a galaxy, while the sticky-particle method is better suited for approximating the cold gas phase (Merlin & Chiosi 2007). In Salo et al. (1999), which address IC 4214, it was estimated that sticky-particle modeling can yield Ω_p within about 10–20%, even when allowing for uncertainties in the bar amplitude (due to unknown vertical extent, unknown dark halo contribution, and possible variations in the mass-to-light ratio (M/L)) and the numerical parameters involved in the sticky-particle method itself. Direct comparisons between pattern speeds derived from sticky-particle and SPH methods of modeling are not published, although a comparison of results from both methods is discussed by Bournaud et al. (2005) in regards to the gravity torques between a stellar bar and gas. It was found that the tree-SPH code by Semelin & Combes (2002) produced the same order value as that in sticky particle simulations and observations.

In this paper, we compare the kinematic bar pattern speeds of NGC 2523 and NGC 4245, measured through the use of the TW method (Treuthardt et al. 2007), to the dynamical bar pattern speeds derived through simulations. In particular, we base our simulation estimates solely on morphological comparisons and check whether Ω_p is consistent with direct measurements. If so, this would justify the application of the simulation method to a large number of galaxies observed in various NIR surveys, which do not necessarily possess such extensive kinematical data as IC 4214. NGC 2523 is an SB(r)b galaxy with a closed inner ring and multiple arms (see Figure 1). A color index map (Buta et al. 2007) shows that the spiral arms and part of the inner ring are sites of recent star formation. NGC 4245 is an SB(r)0/a galaxy with strong nuclear and inner resonance ring features that are also prominent blue features in a Buta et al. (2007) color

Table 1
Simulation Data

Simulation	R_{CR}/R_B	Ω_p (km s^{-1} arcsec^{-1})	Ω_p (km s^{-1} kpc^{-1})[a]
NGC 2523 without halo	2.0	4.1	16.5
	1.9	4.3	17.6
	1.8	4.6	18.8
	1.7	5.0	20.0
	1.6	5.3	21.5
	1.5	5.7	23.1
	1.4	6.2	25.0
	1.3	6.7	27.1
	1.2	7.3	29.5
	1.1	8.0	32.2
	1.0	8.6	34.9
NGC 2523 with halo	1.4	6.2	25.1
NGC 4245 without halo	2.0	1.8	29.9
	1.9	1.9	31.9
	1.8	2.1	34.2
	1.7	2.2	36.8
	1.6	2.4	39.9
	1.5	2.7	43.5
	1.4	2.9	47.7
	1.3	3.2	52.7
	1.2	3.6	58.4
	1.1	4.0	64.8
	1.0	4.4	71.5
NGC 4245 with halo	1.5	2.9	51.5

Note. [a] With an assumed distance of 51.0 Mpc for NGC 2523 and 12.6 Mpc for NGC 4245.

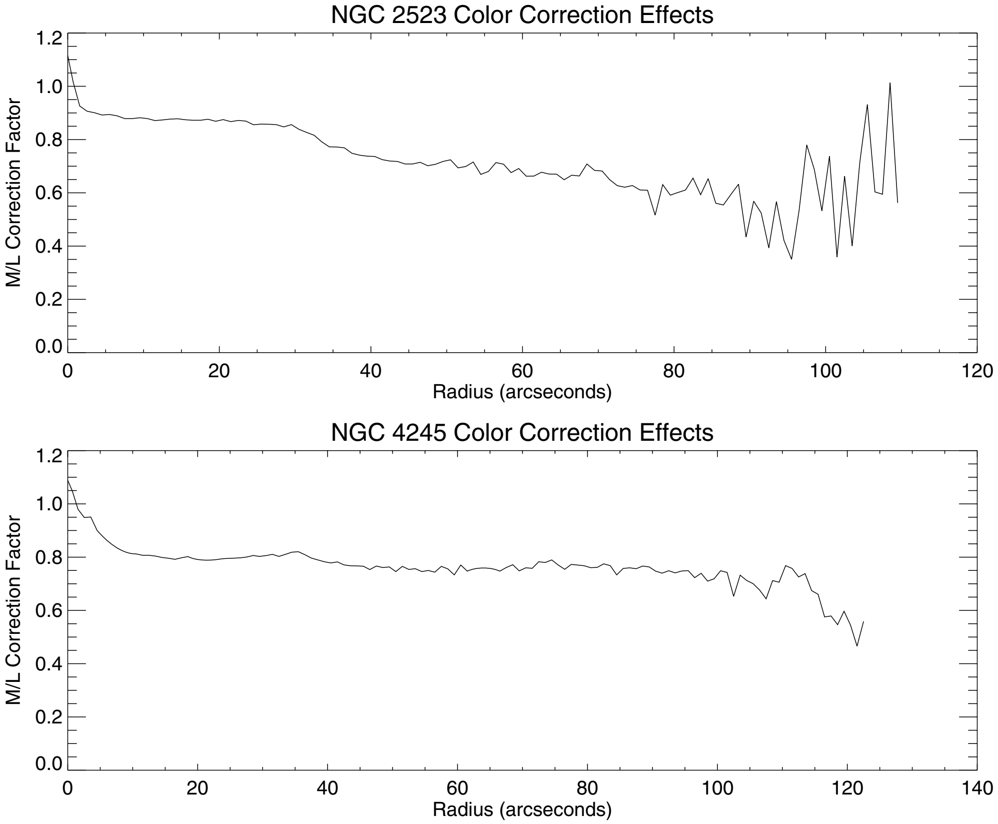

Figure 2. Plots of the radial M/L profiles derived from the formation epoch with bursts model described in Bell & de Jong (2001) for NGC 2523 and NGC 4245.

index map. NGC 4245 is an excellent candidate for such a test due to the good statistical fit of the measured pattern speed. The resonance features apparent in these galaxies help to constrain the dynamical models used to determine the bar pattern speed because the sizes and shapes of the rings are sensitive to the pattern speed. Since gas velocity maps of these galaxies do not exist, we are not able to compare the modeled gas kinematics to observations.

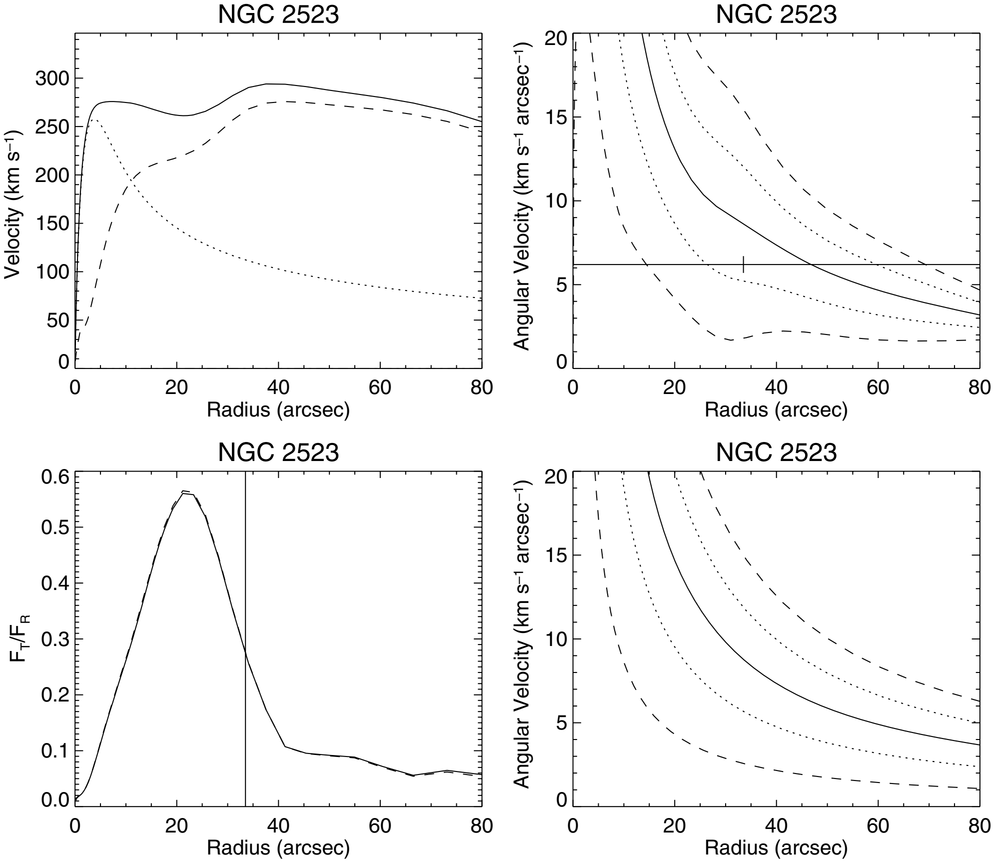

Figure 3. Plots of circular-speed curves, Lindblad precession frequency curves, and the radial variation of the tangential force amplitude (F_T) normalized by the axisymmetric disk force (F_R) for NGC 2523. The upper left panel shows the rotation curve (solid curve) of the galaxy derived from the mass model based on the M/L-corrected K_s-band image. The bulge (dotted curve) and disk components (dashed curve) are also shown. The curves have been scaled so that the maximum rotation velocity is equal to 294 km s^{-1} (Treuthardt et al. 2007). The panels on the right show the precession frequency curves derived from the mass-model rotation curve (upper right) and a constant rotation curve of 294 km s^{-1} (lower right). From left to right, the curves correspond to $\Omega - \kappa/2$, $\Omega - \kappa/4$, Ω, $\Omega + \kappa/4$, $\Omega + \kappa/2$. Ω is the circular angular velocity and κ is the epicyclic frequency. The horizontal line in the upper right panel indicates our best estimate of $\Omega_p = 6.2$ km s^{-1} arcsec^{-1}. The short vertical line corresponds to the error range in Ω_p and is placed at the estimated bar radius of 33″.5. The lower left panel shows the F_T/F_R profile reaching a maximum of 0.56 at approximately 21″ (solid curve). A dashed curve, which nearly coincides with the solid curve, shows the F_T/F_R profile for the case of an added halo component as shown in Figure 10 and discussed in Section 3. The vertical line shows the estimated bar radius.

2. ANALYSIS

2.1. Determining the Potential

In order to simulate the dynamics of the galaxies, a gravitational potential was derived by assuming that the NIR light distribution effectively traces the mass distribution. This assumption is justified since the amount of dark matter within the R_{25} optical disk radius is small compared with the amount of visible matter, allowing maximal disk models to account for the observed rotation (see Quillen et al. 1994 and references therein). The potential may then be derived from the convolution of the density with the function $1/R$ (Quillen et al. 1994), combined with an assumption for the vertical density distribution. For NGC 2523 and NGC 4245, the potentials were derived from 2.15 μm K_s-band images obtained for the Near-Infrared S0 Survey (NIRS0S; Laurikainen et al. 2005, 2006; Buta et al. 2006) in 2003 January with the 2.5 m Nordic Optical Telescope (NOT) and in 2006 May with the 4.2 m William Herschel Telescope, respectively. During the NOT run, B- and V-band images were also taken to help define the orientation parameters of the two galaxies. These values are summarized by Treuthardt et al. (2007).

The K_s-band light distribution is useful for estimating the potential due to the reduced extinction effects from dust and the weakened influence of young Population I complexes. Before the gravitational potential was derived, the K_s-band images were converted into a surface mass density by assuming a M/L that accounts for the average disk V–K_s color gradient using formulae from Bell & de Jong (2001). The "formation epoch with bursts" M/L model listed in Table 1 of Bell & de Jong (2001) was applied to the azimuthally averaged K_s-band images, which were then used to derive a gravitational potential. These color profiles are shown in Figure 2. Note that although it would be ideal to apply M/L corrections on a pixel-by-pixel basis instead of an azimuthal average, the much larger uncertainties on pixel colors makes this less practical. Thus, we are only correcting the axisymmetric backgrounds of the galaxies for stellar M/L effects.

The gravitational potentials were calculated by first using an iterative two-dimensional bulge–disk–bar decomposition identical to that described by Laurikainen et al. (2004). This method models the bulge in terms of a Sérsic $r^{1/n}$ function, the disk in terms of an exponential, and the bar in terms of a Ferrers function. A more sophisticated approach is used by Laurikainen et al. (2006). The parameters are iterated on a sky-subtracted image that is cleaned of foreground and background objects. The bulge component was removed from the K_s-band light distribution and the disk was then deprojected to a face-on

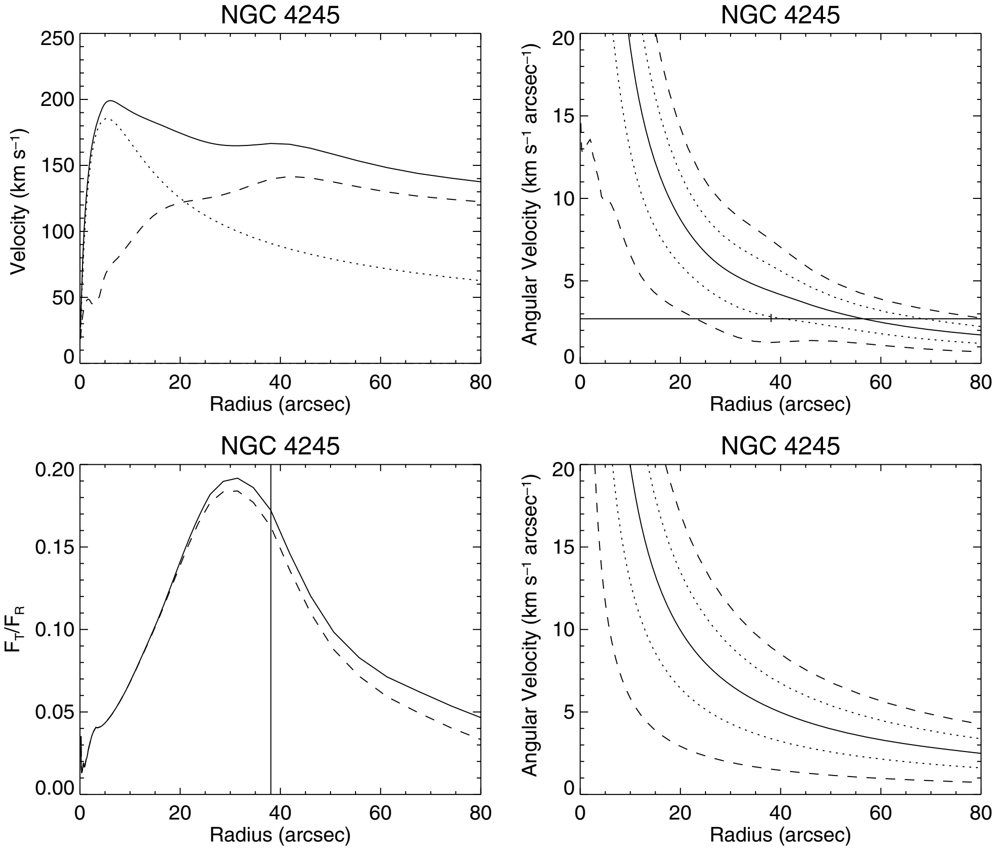

Figure 4. Plots of circular-speed curves, Lindblad precession frequency curves, and the radial variation of the tangential force amplitude (F_T) normalized by the axisymmetric disk force (F_R) for NGC 4245. The upper left panel shows the rotation curve (solid curve) of the galaxy derived from the mass model based on the M/L-corrected K_s-band image. The bulge (dotted curve) and disk components (dashed curve) are also shown. The curves have been scaled so that the maximum rotation velocity is equal to 199 km s^{-1} (Treuthardt et al. 2007). The panels on the right show the precession frequency curves derived from the mass-model rotation curve (upper right) and a constant rotation curve of 199 km s^{-1} (lower right). From left to right, the curves correspond to $\Omega - \kappa/2$, $\Omega - \kappa/4$, Ω, $\Omega + \kappa/4$, $\Omega + \kappa/2$. Ω is the circular angular velocity and κ is the epicyclic frequency. The horizontal line in the upper right panel indicates our best estimate of $\Omega_p = 2.7$ km s^{-1} arcsec^{-1}. The short vertical line corresponds to the error range in Ω_p and is placed at the estimated bar radius of $38''.1$. The lower left panel shows the F_T/F_R profile reaching a maximum of 0.19 at approximately $31''$ (solid curve). The dashed curve shows the F_T/F_R profile for the case of an added halo component as shown in Figure 10 and discussed in Section 3. The vertical line shows the estimated bar radius.

orientation. The disk light distribution was approximated by a Fourier decomposition and the disk gravity was calculated using the even components from $m = 0$ to $m = 8$, as was done by Rautiainen et al. (2005). The odd Fourier components of the disk are small compared with the even components. For example, the maximum relative tangential perturbation F_T/F_R is 0.56 for NGC 2523 when only the even components are taken into account. F_T/F_R increases by approximately 0.02 to 0.58 when the odd Fourier components from $m = 1$ to $m = 9$ are included. Here F_T stands for the amplitude of the tangential force, while F_R is the azimuthally averaged radial force. Typical vertical scale heights of 1/5 and 1/4 of the radial scale length were assumed for the disk components of NGC 2523 and NGC 4245, respectively. These scale heights were selected based on the empirical relation of scale height to radial scale length of a galaxy discussed by de Grijs (1998). Overall, the effect of scale height on F_T/F_R is not large. For example, if the ratio of vertical scale height to radial scale length of NGC 2523 is changed from 1/5 to 1/10, the maximum value of F_T/F_R would change from 0.56 to 0.70. The gravitational potential of the bulge was also added to the disk potential under the assumption that the bulge mass is spherically distributed. A constant M/L scale factor was applied to each potential so that the derived circular-speed curve reached the same maximum velocity used by Treuthardt et al. (2007; see Figures 3 and 4). No gas rotation curves of these galaxies exist for comparison with the modeled circular-speed curves.

2.2. *Simulations*

The simulation code used to model NGC 2523 and NGC 4245 was written by H. Salo, the details of which can be found in Salo et al. (1999; see also Salo 1991 for the treatment of particle impacts). The behavior of a two-dimensional disk of 20,000 inelastically colliding gas particles and 100,000 noncolliding stellar test particles was simulated in the determined potential. The initial particle distribution was exponential and the particle velocities were calculated with the epicyclic approximation, using a radial velocity dispersion amounting to 10% of the circular velocity at each radius. The circular velocity was calculated using the total axisymmetric component of the gravity potential. The nonaxisymmetric potential component of the bar potential was turned on gradually and reached full strength at two bar rotations. The main parameter that was varied was the bar pattern speed. The morphology of the simulated gas distribution was compared to the morphology observed in the B-band image of each galaxy (Treuthardt et al. 2007). We specifically compared the size of the inner ring and the overall structure outside of this ring.

In an effort to increase the signal-to-noise ratio (S/N) of the simulation snapshots at the bar rotation period of interest,

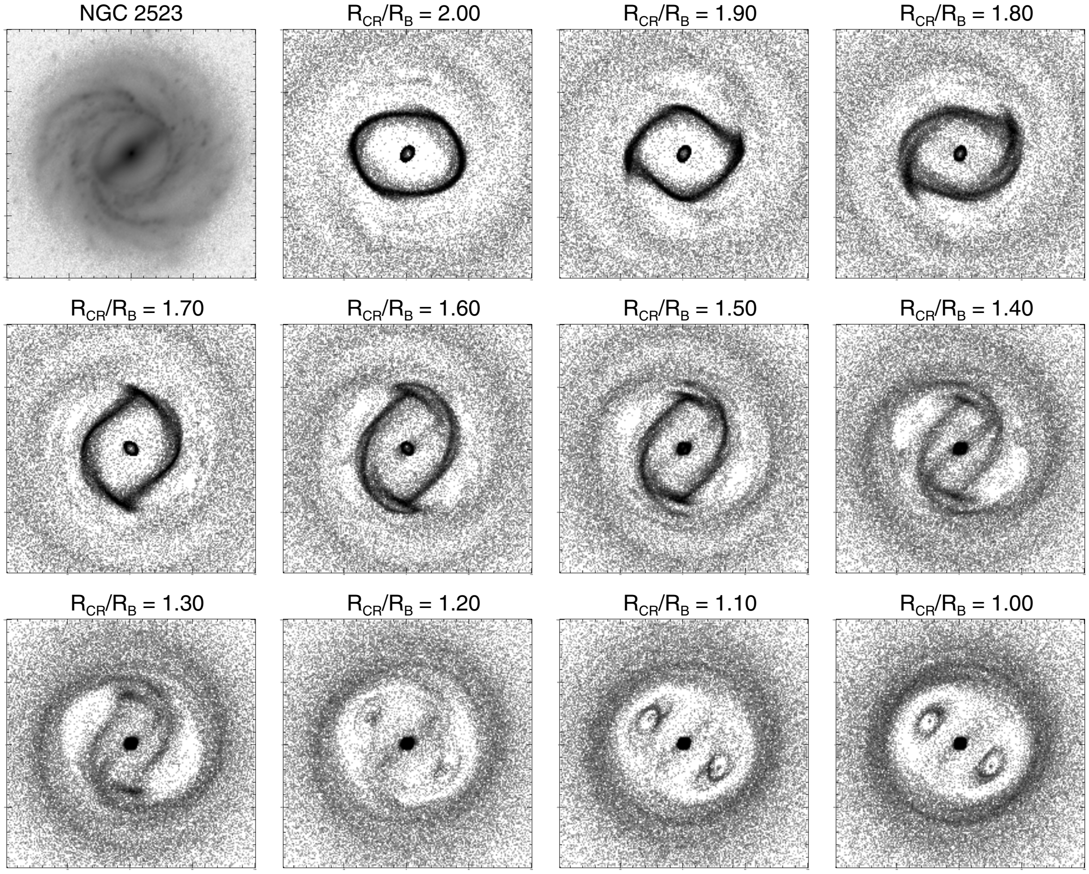

Figure 5. *B*-band, disk-plane image of NGC 2523 (upper left panel) showing the SB(r)b morphology. The remaining panels are gas simulations showing the disk-plane morphology at seven bar rotations for different pattern speeds corresponding to the shown R_{CR}/R_B values. The deprojected value of R_B is 33.″5. Each panel is 200″ × 200″.

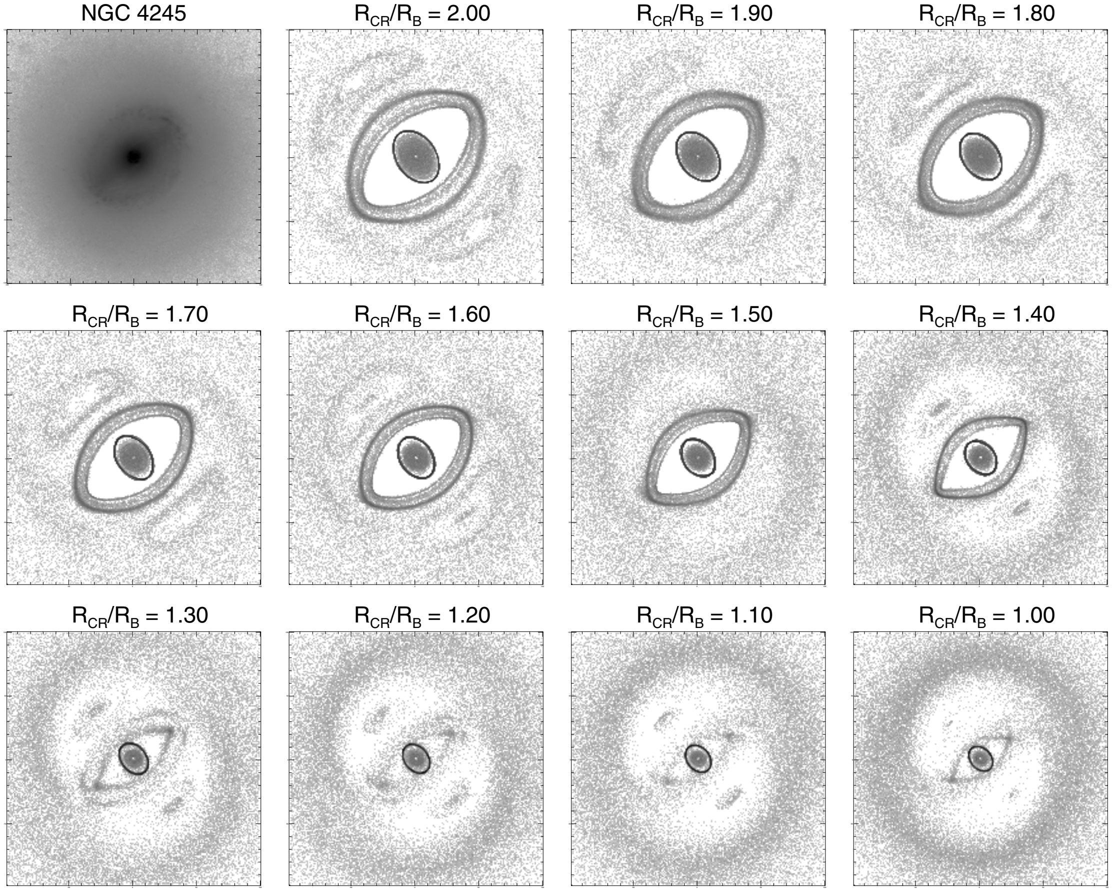

Figure 6. *B*-band, disk-plane image of NGC 4245 (upper left panel) showing the SB(r)0/a morphology. The remaining panels are gas simulations showing the disk-plane morphology at 12 bar rotations for different pattern speeds corresponding to the shown R_{CR}/R_B values. The deprojected value of R_B is 38.″1. Each panel is 200″ × 200″.

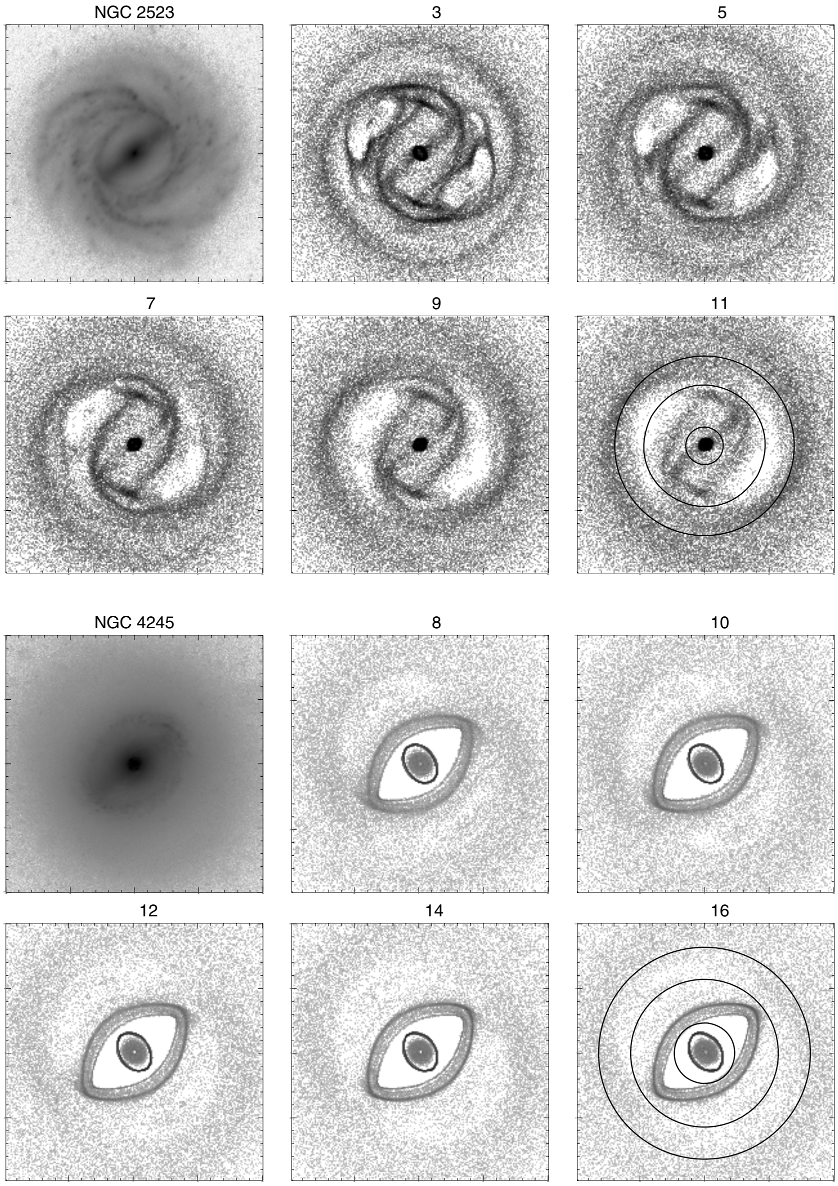

Figure 7. Two sets of six panels comparing the *B*-band with gas simulation morphologies of NGC 2523 (upper set) and NGC 4245 (lower set) in the disk-plane. For NGC 2523, the upper left panel shows the *B*-band SB(r)b morphology. The remaining panels are gas simulations showing the morphology from 3 to 11 bar rotations for a pattern speed corresponding to R_{CR}/R_B of 1.4. For NGC 4245, the upper left panel shows the *B*-band SB(r)0/a morphology. The remaining panels are gas simulations showing the morphology from 8 to 16 bar rotations for a pattern speed corresponding to R_{CR}/R_B of 1.5. The lower right panel in each set has circles overlayed which indicate (from smallest to largest radius) the locations of the inner Lindblad resonance, corotation, and the OLR. Each panel is 200″ × 200″.

we aligned and coadded particle snapshots within ±0.2 bar rotation periods in 0.1 bar rotation period increments. The net result is a snapshot of 100,000 gas and 500,000 star particles at a specified bar rotation period. This can be done because after the initial transient evolution related to the turn-on of the bar, the morphology of the simulated galaxies does not change significantly on such a relatively small timescale. In practice, the results were indistinguishable from that which results from using a five-fold number of actual particles of appropriately reduced size to keep the impact frequency constant.

The pattern speed of the simulated galaxies was varied in such a way that the ratio of the corotation radius (R_{CR}) to the bar radius (R_B) ranged from 2.0 to 1.0 in increments of 0.1 (see Table 1). The deprojected bar radius was estimated to be 33″.5 for NGC 2523 and 38″.1 for NGC 4245 (Treuthardt et al. 2007). In Figures 3 and 4 (upper right), we plot the Lindblad precession frequency curves derived from the simulated circular-speed curves estimated from the K_s-band images of the galaxies. These curves show how resonance locations vary with angular velocity in the linear (epicyclic) approximation.

It should be noted that these simulations assume that a single pattern speed is present, when in fact many galaxies may have multiple pattern speeds. Pfenniger & Norman (1990) suggested that nuclear bars represent independent instabilities that could have their own pattern speeds. There is evidence for this in the random alignments observed between primary and secondary bars (e.g., Buta & Crocker 1993; Wozniak et al. 1995; Friedli et al. 1996) and even from direct observations (e.g., Corsini et al. 2003). Sellwood & Sparke (1988) showed that in their *n*-body simulations of naturally forming bars and spirals, the spirals tend to have a lower pattern speed than the bar. More recently, Rautiainen & Salo (1999, 2000) examined the effect

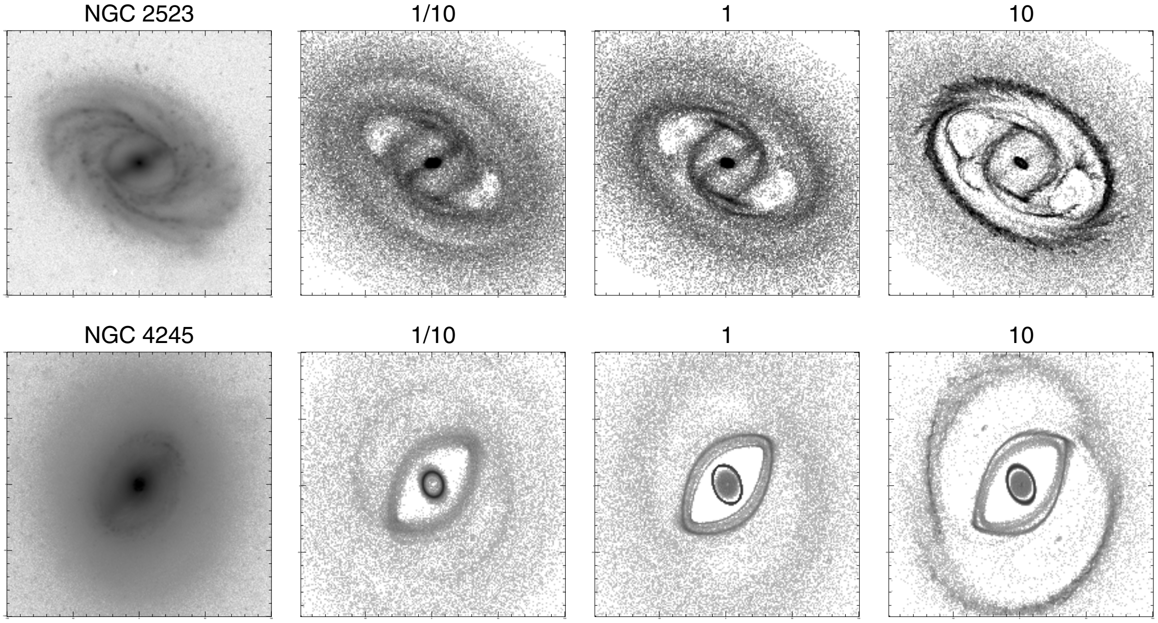

Figure 8. Examples of the difference in morphology of the simulated galaxies when using different particle sizes. The leftmost panels show a *B*-band image of NGC 2523 (upper) and NGC 4245 (lower). The remaining panels show the simulated gas particle morphology of the galaxy at seven bar rotations and R_{CR}/R_B equal to 1.4 for NGC 2523, and 12 bar rotations and R_{CR}/R_B equal to 1.5 for NGC 4245. The particle radii used were, from left to right, 1/10, 1, and 10 times our standard of 1×10^{-2} arcsec.

of multiple pattern speeds in barred galaxies over a Hubble time and with respect to the ring formation. Their simulations demonstrated that the presence of several patterns at the region of the outer Lindblad resonance (OLR; $\Omega_p = \Omega + \kappa/2$, where Ω is the circular angular velocity and κ is the epicyclic frequency) does not inhibit the formation of an outer ring, but can cause cyclic changes in its morphology (Figure 10 in Rautiainen & Salo 2000). However, even when slower modes are present and affect the shape of the outer ring, the ring seems to be related to the OLR of the bar, that is the ring size accommodates the change in OLR distance due to bar slow-down. Nevertheless, we conclude that the possibility of multiple pattern speeds is not a serious limitation on our study because our focus is on the bars and morphology immediately surrounding and outside the bars.

3. RESULTS AND DISCUSSION

In order to estimate Ω_p for these galaxies, we would like to find the Ω_p value that best visually matches the simulated and observed morphologies. Because of their smaller velocity dispersion compared with stars, gas morphology is more sensitive to Ω_p. Since *B*-band images tend to show details of gas morphology, our visual comparisons will be between models and *B*-band images. Note that factors other than Ω_p affect the morphology of a simulated galaxy. These factors include the time when the features are examined, impact frequency from the assumed cross section of the particles, contribution of a possible dark halo component, and the strength of F_T/F_R via the assumed vertical profile.

Figures 5 and 6 show the effect of different bar pattern speeds (or R_{CR}/R_B values), at an equal number of bar rotation periods, on the morphologies of NGC 2523 and NGC 4245, respectively. In the case of NGC 2523, larger values of Ω_p (corresponding to smaller values of R_{CR}/R_B; see Table 1) cause the inner ring to become smaller and less oval until it is no longer able to form. When $R_{\mathrm{CR}}/R_B = 1.4$, a gaseous bar is clearly apparent, the inner ring is approximately the same size as seen in the *B*-band, and the simulated morphology outside of the inner ring resembles that of the observed galaxy. In the case of NGC 4245, larger values of Ω_p also cause the inner ring to become smaller until it is no longer able to form. When R_{CR}/R_B is 1.6 or greater, the so-called “banana” orbits are apparent, while when R_{CR}/R_B is 1.4 or less, the L_4 and L_5 Lagrangian point regions are nearly cleared of gas except for some small collections of particles.

The evolution of the simulated morphologies of NGC 2523 and NGC 4245 is shown in Figure 7. Here, a single Ω_p is examined at a different number of bar rotation periods. In the case of NGC 2523, the gas morphology of the simulation appears settled after about four bar rotations while the sharp features appear to slowly diffuse. In the case of NGC 4245, the gas morphology appears settled after about eight bar rotations, but the L_4 and L_5 regions continue to be cleared of particles. As an aside, we changed the number of simulation steps per orbit in order to examine the effects on the models of NGC 2523. We found that changing our standard of approximately 350 steps per orbit at the bar radius ($33\overset{\prime\prime}{.}5$) to 700 steps per orbit did not produce a noticeably different morphology.

The effect of the particle impact frequency on the simulated morphology of the galaxies is shown in Figure 8. Here, we see how the morphology changes when the gas particle radius of 1×10^{-2} arcsec is changed by a factor of 1/10, 1, and 10. As the particle cross section increases, the impact frequency also increases and the gaseous features become sharper and well defined. For NGC 2523, the similarity in morphology between the observation and the model, which uses our nominal particle cross section, is not as apparent when the cross section is changed by an order of magnitude. The typical impact frequencies of the inner and outer ring regions of this galaxy, using our nominal particle cross section, are 1.5 and 0.8 impacts per particle per bar rotation, respectively. For NGC 4245, the

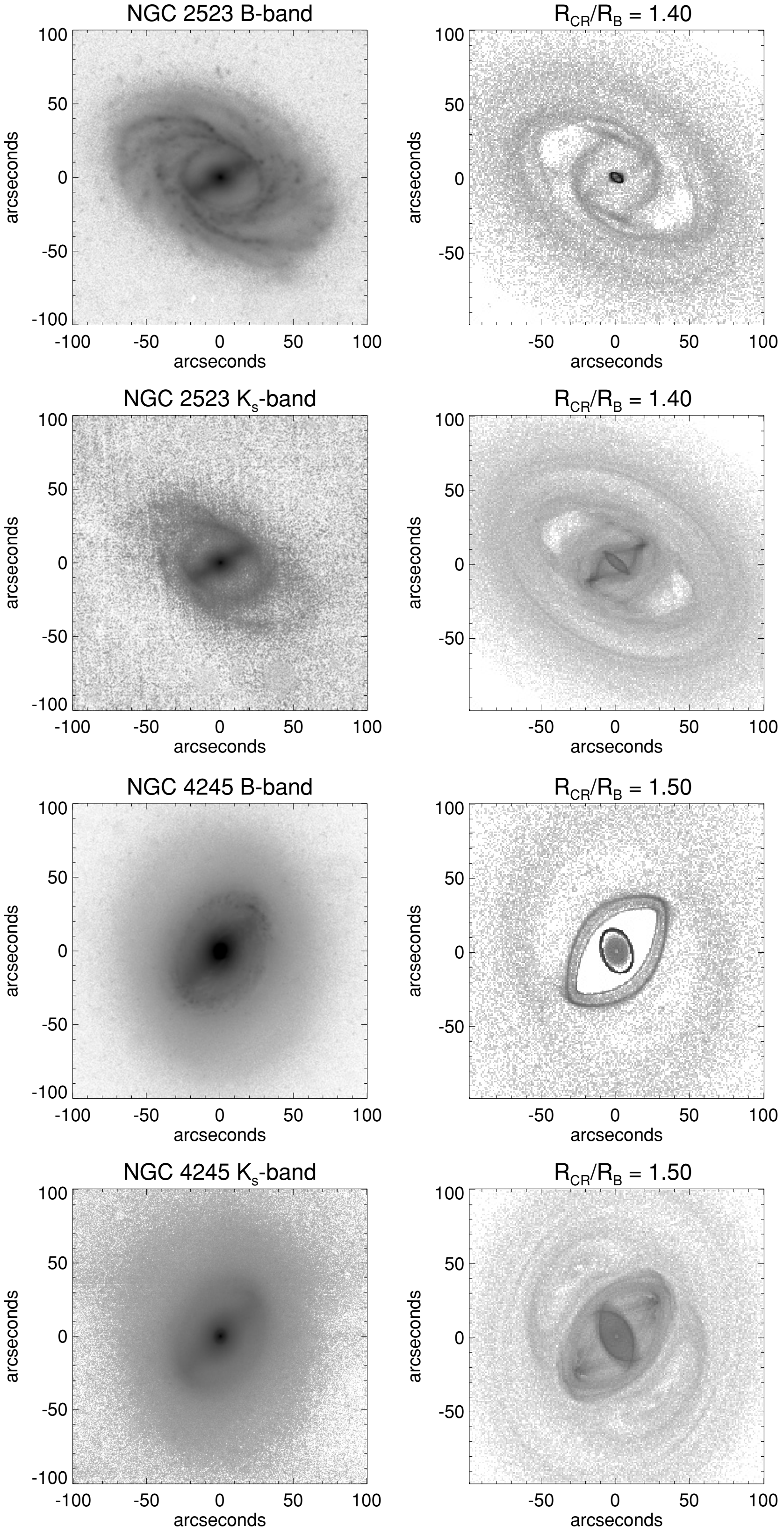

Figure 9. Images showing the observed and simulated morphologies of NGC 2523 (upper four plots) and NGC 4245 (lower four plots). The B-band (upper left), simulated gas (upper right), K_s-band (lower left), and simulated stellar morphologies (lower right) of each galaxy are displayed. The simulated gas and stellar morphologies of NGC 2523 are shown at seven bar rotations with $R_{\rm CR}/R_B = 1.4$ and no additional halo. The simulated gas and stellar morphologies of NGC 4245 are shown at 12 bar rotations with $R_{\rm CR}/R_B = 1.5$ and no additional halo. The simulated morphologies correspond to our best simulations. The initial radial velocity dispersion of both the gas and stellar test particles is 10% of the circular velocity. The stellar test particles are noncolliding, unlike the gas particles.

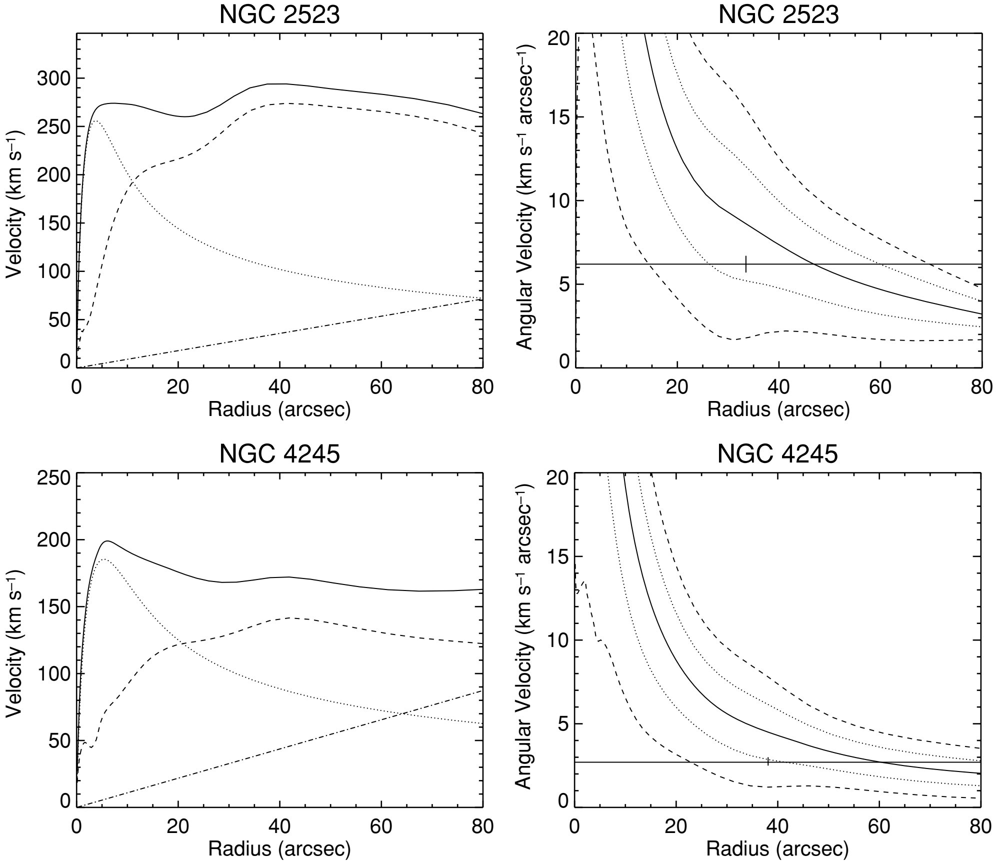

Figure 10. Plots shown here are similar to the upper plots in Figures 3 and 4, but with the addition of a halo component. The halo contribution to the total circular-speed curve is shown as the dot-dashed curve in the plots on the left. The corresponding Lindblad precession frequency curves are shown on the right.

typical impact frequencies of the inner and outer ring regions are 1.4 and 0.4 impacts per particle per bar rotation, respectively. When the impact frequencies are much less than 1 impact per particle per bar rotation the morphology approaches that of noncolliding test particles. This is evident when comparing the morphology of the galaxies using $1/10$ the nominal particle radius in Figure 8 with the stellar test particle morphology in Figure 9. If the initial distribution of particles is uniform instead of exponential, the impact frequencies would increase in the outer parts of the galaxy relative to the inner parts.

The simulations shown thus far do not include a dark halo component. The inclusion of a halo also has implications in the morphology of the simulations. In Figure 10, we show the effect of a halo component, based on the universal rotation curve of Persic et al. (1996), on the circular-speed curve and Lindblad precession frequency curves of NGC 2523 and NGC 4245. The added halos were assumed to be isothermal spheres with core radii of 147″ and 83″ and asymptotic velocities of 159 km s^{-1} and 137 km s^{-1} for NGC 2523 and NGC 4245, respectively. The mass of the halo component of NGC 4245 was scaled by approximately $1/3$, with respect to the universal rotation curve model, in order to prevent the total circular-speed curve from rising significantly at large radii ($r > 60''$). A constant M/L scale factor was again applied to each potential so that the derived rotation curve reached the same maximum velocity used by Treuthardt et al. (2007). In Figure 11, the effects of the halo component are shown for $R_{\mathrm{CR}}/R_B = 1.4$ and 1.5 for NGC 2523 and NGC 4245, respectively. In the case of NGC 2523, the halo contribution has no significant effect on the morphology of the galaxy. In the case of NGC 4245, there is significant structure outside the inner ring. Gas particles appear to collect into prominent "banana" orbits. The reduced perturbation does not lead to the clearing of L_4 and L_5 as seen in the models without a halo.

We also examine the effects of varying the bar amplitude, without adding a halo, on the modeled gas morphology of the galaxies in Figures 12 and 13. In these models, the nonaxisymmetric Fourier components of the potential were multiplied by a factor while the axisymmetric component was kept intact. We examine models using our best estimate of Ω_p found in this paper and the average Ω_p estimated by Treuthardt et al. (2007). The bar amplitude is varied from a factor of 1.25–0.25. These models serve to describe the possible effects of uncertainties in elements such as the bar height and halo contribution. A comparison of the total circular-speed curves of NGC 4245 in Figures 4 and 10 suggests that the total radial force increases by approximately 1.4 times at 80″ with the addition of our halo component. This corresponds to a reduction in F_T/F_R by a factor of approximately 0.71. Therefore, our models created using different bar amplitudes explore a wider range of uncertainties in the halo contribution than in Figure 11.

In the case of NGC 2523 using the best estimate of Ω_p found in this paper, an inner ring does not form when a bar amplitude factor of 1.25 is applied. A factor of 0.75 produces an inner ring that appears somewhat stretched along the galaxy MA. A gas bar is not produced and the outer spiral arms are more clearly defined compared to the model using a factor of 1.00. Models produced using bar amplitude factors of less than 0.75 have morphologies that are clearly dissimilar to what is observed. Using the average Ω_p estimated by Treuthardt et al. (2007) and different bar

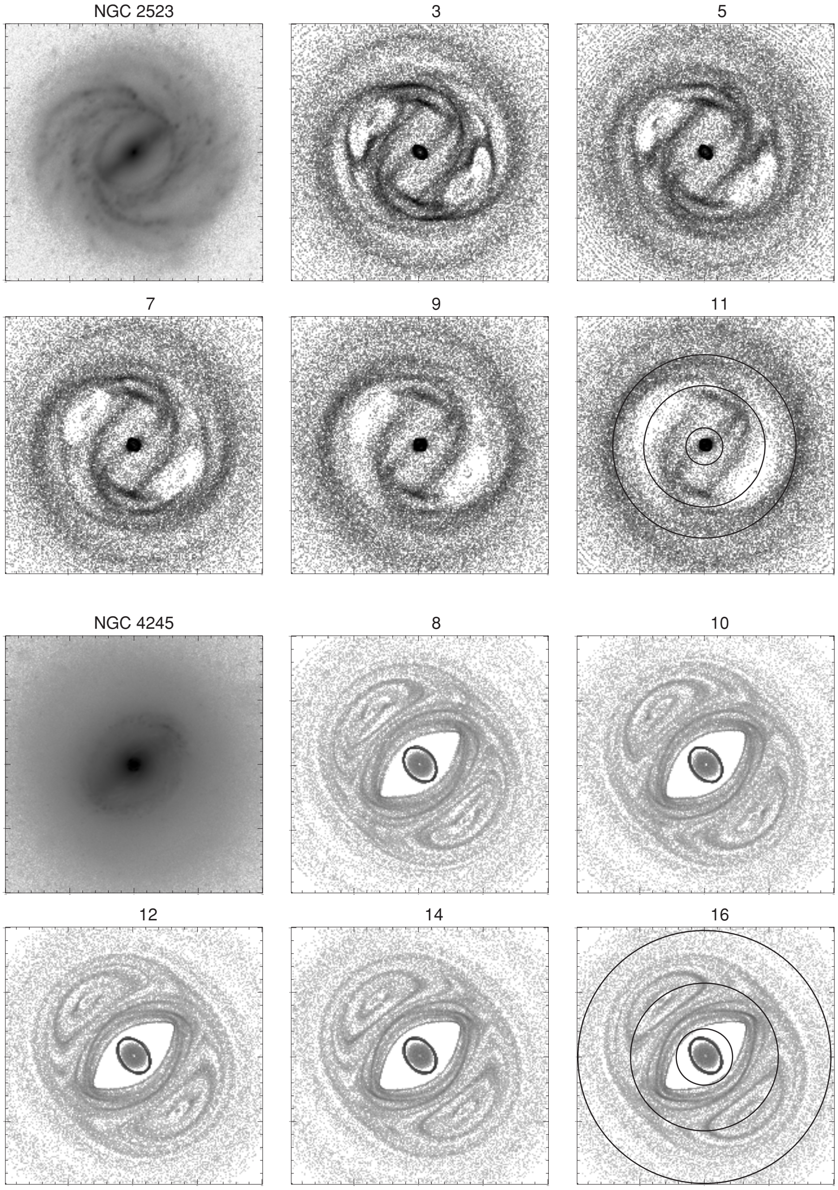

Figure 11. Plots similar to those shown in Figure 7 only with the contribution of a halo component (shown in Figure 10) taken into account.

amplitude factors, the models do not display morphology similar to what is observed in the *B* band. Most significantly, the inner ring shape does not match the observations in any case. Based on these results, it appears that our best estimate of Ω_p, along with a bar that is slightly weaker than our nominal value, recreates the observed morphology most accurately.

Using the best estimate of Ω_p found in this paper for NGC 4245, we find that a bar amplitude factor of 1.25 produces an inner ring that is thinner and slightly more elliptical than what is seen in both our nominal case and the *B*-band image. Models with a bar amplitude factor of less than 1.00 produce thicker inner rings and show "banana" orbits, along with other structure, outside the inner ring region that is not observed in the galaxy. Models produced using the average Ω_p estimated by Treuthardt et al. (2007) and different bar amplitude factors have inner ring morphologies that are clearly dissimilar to the observations. Although the error limits of this observationally derived Ω_p estimate are large, this could be an indication of multiple pattern speeds. The TW method is more likely to measure the innermost pattern speed since the S/N is higher. This leads us to believe that our model with the best estimate of Ω_p and nominal bar amplitude are correct.

Table 2

Pattern Speed Estimates

Galaxy	$\Omega_p{}^{\mathrm{a,b}}$ (Treuthardt et al. 2007)	$\Omega_p{}^{\mathrm{a}}$ (Dynamical Simulation)
NGC 2523	6.6 ± 1.6	$6.2^{+0.5}_{-0.5}$
NGC 4245	4.7 ± 1.9	$2.7^{+0.3}_{-0.2}$

Notes.

[a] km s^{-1} arcsec^{-1}.

[b] Inclinations of 49°.7 for NGC 2523 and 35°.4 for NGC 4245 were assumed in these values.

For NGC 2523, good agreement between the observed and simulated size of the inner ring and morphology outside this ring is obtained with $R_{\mathrm{CR}}/R_B = 1.4 \pm 0.1$ (see Figures 5 and 9).

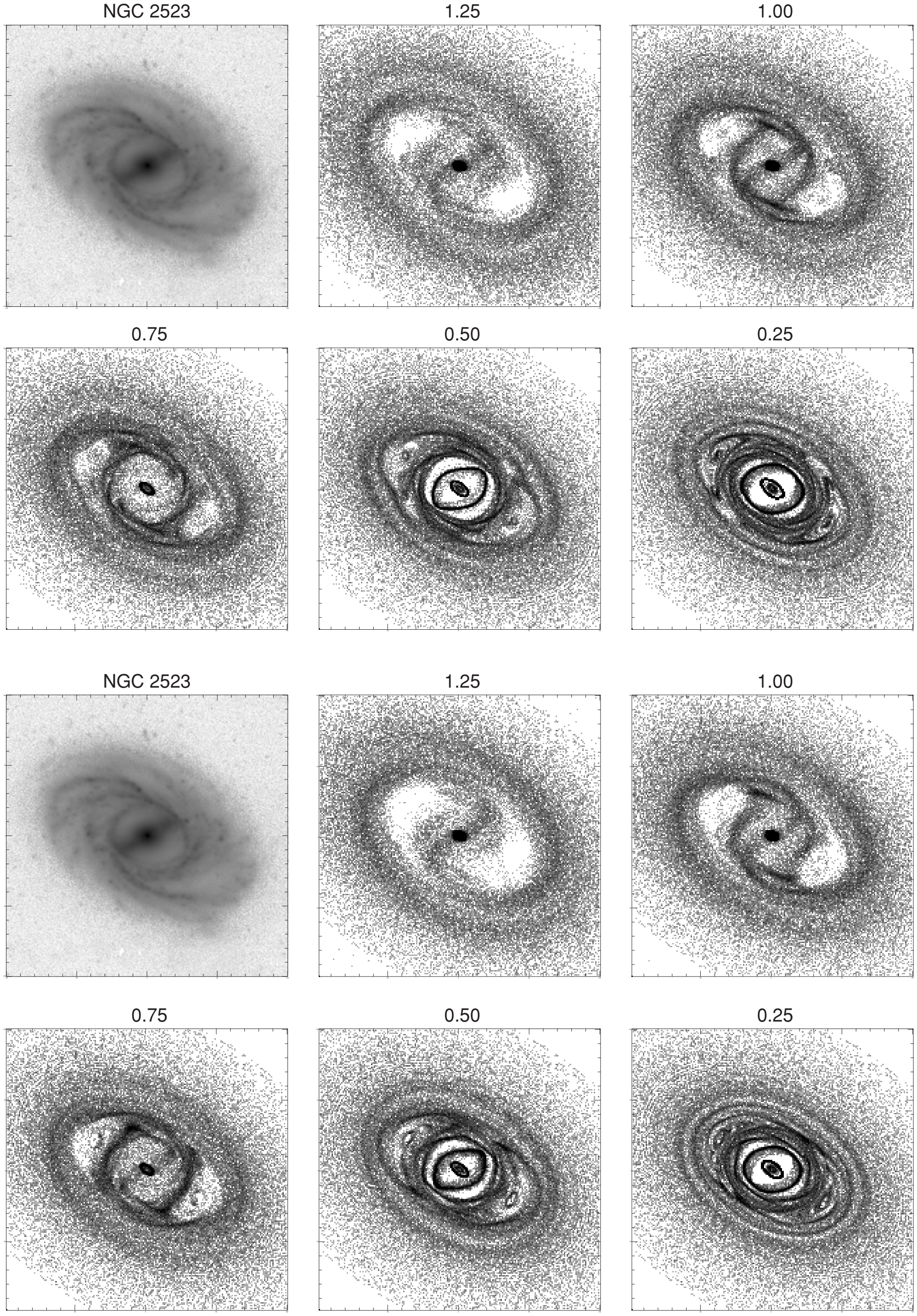

Figure 12. Images showing the morphological effects of applying different bar amplitudes to models of NGC 2523. The top two rows compare the *B*-band image (upper left) with our best model ($\Omega_p = 6.2$ km s^{-1} arcsec^{-1} and seven bar rotations), with the bar amplitude varying from 1.25 to 0.25. The bottom two rows compare the *B*-band image with models using the average pattern speed found by Treuthardt et al. (2007; $\Omega_p = 6.6$ km s^{-1} arcsec^{-1} and seven bar rotations), with the bar amplitude also varying from 1.25 to 0.25.

This corresponds to a pattern speed of $6.2^{+0.5}_{-0.5}$ km s^{-1} arcsec^{-1}, or $25.0^{+2.0}_{-2.0}$ km s^{-1} kpc^{-1} with an assumed distance of 51.0 Mpc (Kamphuis et al. 1996). For NGC 4245, agreement is obtained with $R_{\rm CR}/R_B = 1.5 \pm 0.1$ (see Figures 6 and 9). This corresponds to a pattern speed of $2.7^{+0.3}_{-0.2}$ km s^{-1} arcsec^{-1}, or $43.5^{+4.9}_{-3.3}$ km s^{-1} kpc^{-1} with an assumed distance of 12.6 Mpc (García-Barreto et al. 1994). These Ω_p values agree within the errors, though marginally, with the values determined by Treuthardt et al. (2007) through the completely independent TW method (see Table 2). In Table 3, we list the inferred resonance locations for our best-fitting models. We also compare the observed and modeled ring MA radii and axis ratios.

Our best simulations do not match the observed morphologies exactly. The simulated inner region of NGC 2523 shows gas particles collecting near the ends of the bar, close to the inner ring, which could be interpreted as regions of star formation (see Figure 9). There is no such star formation evident in the

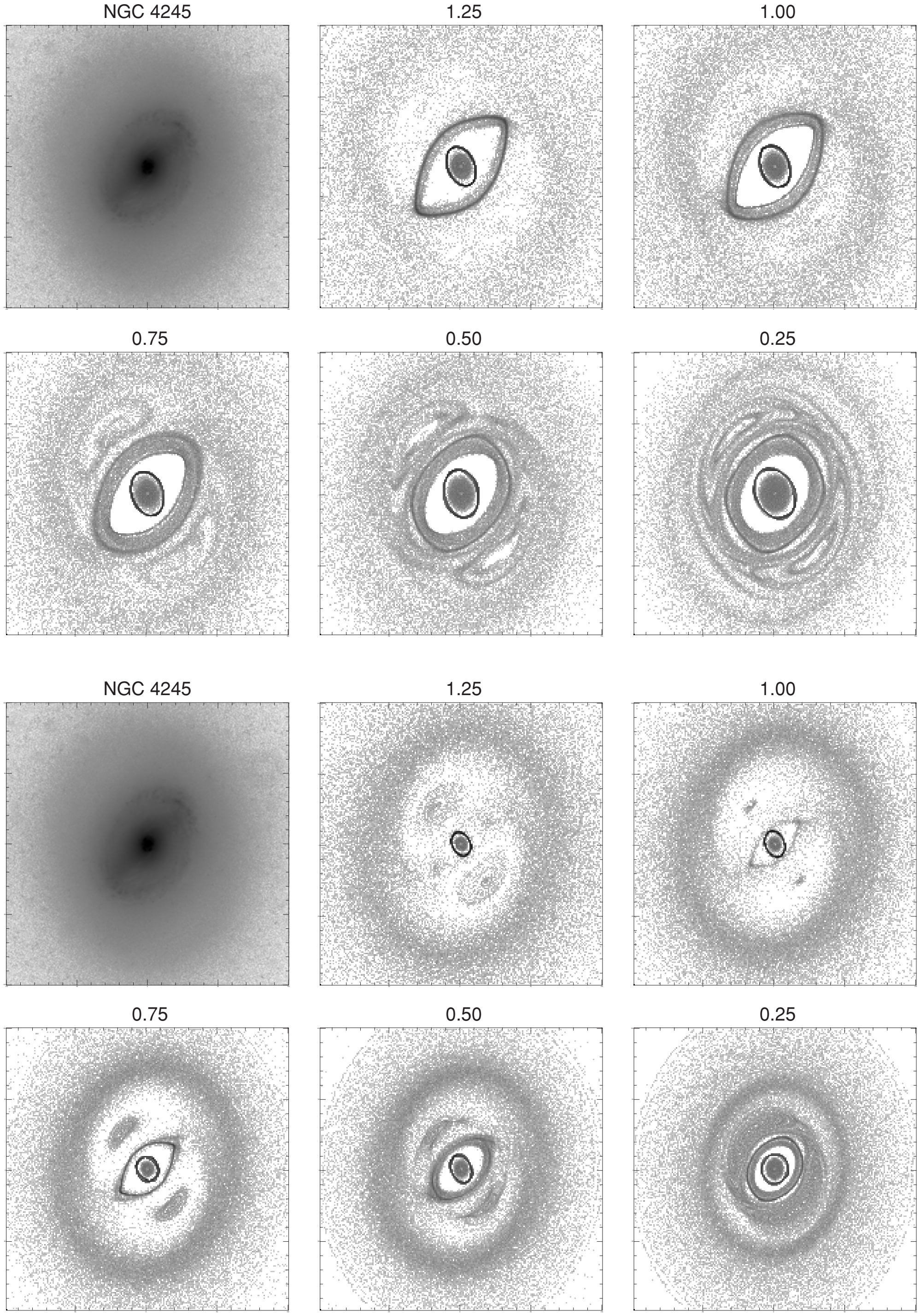

Figure 13. Images showing the morphological effects of applying different bar amplitudes to models of NGC 4245. The top two rows compare the B-band image (upper left) with our best model ($\Omega_p = 2.7$ km s^{-1} arcsec^{-1} and 12 bar rotations), with the bar amplitude varying from 1.25 to 0.25. The bottom two rows compare the B-band image with models using the average pattern speed found by Treuthardt et al. (2007; $\Omega_p = 4.7$ km s^{-1} arcsec^{-1} and 12 bar rotations), with the bar amplitude also varying from 1.25 to 0.25.

observed bar of NGC 2523. The structure outside the observed inner ring of NGC 2523 is complicated and slightly asymmetric, whereas the simulated morphology is necessarily bisymmetric since only even m values were used to calculate the disk gravity. A comparison of the simulated stellar and K_s-band morphology shows even less of a similarity. The main families of periodic stellar orbits, x_1 and x_2, are easily recognized in the simulated morphology of the galaxy but are indiscernible in the observed stellar image. In general, the bar-supporting x_1 family of orbits will not extend beyond the corotation radius of a galaxy, which places an upper limit on the bar pattern speed. For NGC 2523, these orbits appear to extend the length of the bar, which is expected.

The obvious difference between our best simulation and the observed B-band morphology of NGC 4245 is within the inner ring. The simulation produces a nuclear ring approximately 3.3 times larger than what is seen in the B band (see Table 3 and Figure 9). A faster pattern speed produces a nuclear ring more

Table 3
Galaxy Resonance and Ring Properties[a]

Galaxy (1)		ILR (2)	CR (3)	OLR (4)	a_n (5)	$(b/a)_n$ (6)	a_i (7)	$(b/a)_i$ (8)
NGC 2523	Model[b]	14″.5	47″.0	69″.5	n/a	n/a	38″ ± 4″	0.66 ± 0.13
	Observation[c]				n/a	n/a	35″.3	0.74
NGC 4245	Model[d]	23″.5	57″.2	82″.0	16″ ± 1″	0.75 ± 0.08	46″ ± 5″	0.61 ± 0.13
	Observation[c]				4″.8	0.92	40″.6	0.77

Notes.

[a] Explanation of columns: (1) galaxy name; (2) inner Lindblad resonance (ILR) radius; (3) corotation radius; (4) OLR radius; (5) nuclear ring MA radius; (6) nuclear ring axis ratio; (7) inner ring MA radius; (8) inner ring axis ratio. All of the values are in the disk-plane of the galaxy.

[b] Best-fitting model with no halo, $R_{\rm CR}/R_B = 1.4$, and at seven bar rotations.

[c] Parameters from Treuthardt et al. (2007).

[d] Best-fitting model with no halo, $R_{\rm CR}/R_B = 1.5$, and at 12 bar rotations.

similar in size to the observed ring, but the external structures are vastly different. It is possible that the observed morphology is due to more than one pattern speed (Rautiainen et al. 2005), which is not accounted for in our models. Additionally, outside the simulated inner ring is a diffuse outer ring that is not obvious in the observed image. Even our models that include a halo show an outer ring (see Figure 11). It was noted by Treuthardt et al. (2007) that NGC 4245 is one of the more H I-deficient galaxies in the Coma I group and that gas stripping might explain the lack of an observed outer ring. Our models do not account for such an interaction with the galaxy's environment. The simulated stellar and K_s-band morphology of this galaxy appear nearly as dissimilar as they did for NGC 2523. Both the stellar x_1 and x_2 orbits are recognizable in the simulated morphology, but are likewise indiscernible in the K_s-band image. The bar-supporting x_1 family of orbits appear to extend the length of the bar. The simulated stellar component also displays faint "banana" orbits that are not seen in the observations. However, these comparisons with noncolliding test particles should not be taken too literally, as no attempt was made to match their velocity distributions with observations. Rather, they serve to illustrate the extent of various orbital families.

4. CONCLUSIONS

Using NIR images to trace the stellar disk potential, we have estimated the pattern speeds and resonance locations of NGC 2523 and NGC 4245 using the numerical simulation method of Salo et al. (1999; see also Rautiainen et al. 2005). This is completely independent of the approach used by Treuthardt et al. (2007). We have examined the effects of varying the bar pattern speed (or $R_{\rm CR}/R_B$), number of bar rotation periods, number of simulation steps per orbit, particle cross section, halo contribution, and bar amplitude on the simulated galaxy morphology. Our best models were chosen based on the closest match between the observed B-band and modeled morphology. In particular, we compared the sizes of the inner rings and the morphologies outside of the rings. Our best simulation model provides an interpretation of NGC 2523 which places corotation at 1.4 ± 0.1 times the estimated bar radius of 33″.5, consistent with the results of Treuthardt et al. (2007). For NGC 4245, a similar model gives corotation at 1.5 ± 0.1 times the estimated bar radius of 38″.1, which marginally agrees with the results of Treuthardt et al. (2007), within the errors. The values we derived through simulation modeling are robust against the various parameters examined.

Dynamical simulations are of great value as a means of estimating pattern speeds because they are more widely applicable than the TW method. Galaxies where the TW method is not appropriate, due to unfavorable inclinations or bar–disk position angles, can still be simulated to determine Ω_p. Thus, as further tests like ours are made, reliable pattern speeds will become available for larger numbers of galaxies.

P. Treuthardt and R. Buta acknowledge the support of NSF grants AST-0205143 and AST-0507140 to the University of Alabama. H. Salo acknowledges the support of the Academy of Finland. We thank E. Laurikainen and J. H. Knapen for the NIRS0S K_s-band images that we used for our simulations.

REFERENCES

Aguerri, J. A. L., Debattista, V. P., & Corsini, E. M. 2003, MNRAS, 338, 465
Bell, E., & de Jong, R. 2001, ApJ, 550, 212
Bournaud, F., Combes, F., & Semelin, B. 2005, MNRAS, 364, L18
Buta, R. J., & Combes, F. 1996, Fundam. Cosm. Phys., 17, 95
Buta, R. J., Corwin, H. G., & Odewahn, S. C. 2007, The de Vaucouleurs Atlas of Galaxies, (Cambridge: Cambridge Univ. Press)
Buta, R., & Crocker, D. A. 1993, AJ, 105, 1344
Buta, R., Laurikainen, E., Salo, H., Block, D. L., & Knapen, J. H. 2006, AJ, 132, 1859
Canzian, B. 1993, ApJ, 414, 487
Corsini, E. M., Debattista, V. P., & Aguerri, J. A. L. 2003, ApJ, 599, L29
Debattista, V. P. 2003, MNRAS, 342, 1194
Debattista, V. P., Corsini, E. M., & Aguerri, J. A. L. 2002, MNRAS, 332, 65
de Grijs, R. 1998, MNRAS, 299, 595
Egusa, F., Sofue, Y., & Nakanishi, H. 2004, PASJ, 56, L45
Friedli, D., Wozniak, H., Rieke, M., Martinet, L., & Bratschi, P. 1996, A&AS, 118, 461
García-Barreto, J. A., Downes, D., & Huchtmeier, W. K. 1994, A&A, 288, 705
Gerssen, J., & Debattista, V. P. 2007, MNRAS, 378, 189
Gerssen, J., Kuijken, K., & Merrifield, M. R. 1999, MNRAS, 306, 926
Gerssen, J., Kuijken, K., & Merrifield, M. R. 2003, MNRAS, 345, 261
Hernandez, O., Wozniak, H., Carignan, C., Amram, P., Chemin, L., & Daigle, O. 2005, ApJ, 632, 253
Kamphuis, J. J., Sijbring, D., & van Albada, T. S. 1996, A&AS, 116, 15
Laurikainen, E., Salo, H., & Buta, R. 2005, MNRAS, 362, 1319
Laurikainen, E., Salo, H., Buta, R., Knapen, J., Speltincx, T., & Block, D. 2006, AJ, 132, 2634
Laurikainen, E., Salo, H., Buta, R., & Vasylyev, S. 2004, MNRAS, 355, 1251
Levinson, F. H., & Roberts, W. W., Jr. 1981, ApJ, 245, 465
Merlin, E., & Chiosi, C. 2007, A&A, 473, 733
Merrifield, M. R., & Kuijken, K. 1995, MNRAS, 274, 933
Persic, M., Salucci, P., & Stel, F. 1996, MNRAS, 281, 27
Pfenniger, D., & Norman, C. 1990, ApJ, 363, 391
Puerari, I., & Dottori, H. 1997, ApJ, 476, L73
Quillen, A. C., Frogel, J. A., & Gonzalez, R. A. 1994, ApJ, 437, 162
Rautiainen, P., & Salo, H. 1999, A&A, 348, 737
Rautiainen, P., & Salo, H. 2000, A&A, 362, 465

Rautiainen, P., Salo, H., & Laurikainen, E. 2005, ApJ, 631, L129
Salo, H. 1991, A&A, 243, 118
Salo, H., Rautiainen, P., Buta, R., Purcell, G. B., Cobb, M. L., Crocker, D. A., & Laurikainen, E. 1999, AJ, 117, 792
Sellwood, J. A., & Sparke, L. S. 1988, MNRAS, 231, 25
Semelin, B., & Combes, F. 2002, A&A, 388, 826
Tremaine, S., & Weinberg, M. D. 1984, ApJ, 282, L5, (TW)
Treuthardt, P., Buta, R., Salo, H., & Laurikainen, E. 2007, AJ, 134, 1195
Weiner, B. J., Sellwood, J. A., & Williams, T. B. 2001, ApJ, 546, 931
Wozniak, H., Friedli, D., Martinet, L., Martin, P., & Bratschi, P. 1995, A&AS, 111, 115
Zhang, X., & Buta, R. 2007, AJ, 133, 2584